In vitro bone metastasis dwelling in a 3D bioengineered niche

Weijing Han, Rania El Botty, Elodie Montaudon, Laurent Malaquin, Frederic Deschaseaux, Nicolas Espagnolle, Elisabetta Marangoni, Paul Cottu, Gérard Zalcman, Maria Carla Parrini, et al.

In vitro bone metastasis dwelling in a 3D bioengineered niche

Weijing Han[1,7 **], Rania El Botty[2], Elodie Montaudon[2], Laurent Malaquin[3], Frederic Deschaseaux[4], Nicolas Espagnolle[4], Elisabetta Marangoni[2], Paul Cottu[5], Gérard Zalcman[1,6], Maria Carla Parrini[1], Franck Assayag[2], Luc Sensebe[4+], Pascal Silberzan[7], Anne Vincent-Salomon[8], Dutertre Guillaume[9], Sergio Roman-Roman[10], Stephanie Descroix [7,*], and Jacques Camonis [1,*]

1. Institut Curie, Centre de Recherche, Paris Sciences et Lettres Research University, 75005 Paris, France; ART group, Inserm U830, 75005 Paris, France
2. Laboratory of Preclinical Investigation, Translational Research Department, Institut Curie, PSL Research University, 75005 Paris, France
3. LAAS-CNRS, Université de Toulouse, CNRS, F-31400, Toulouse, France
4. STROMALab, Etablissement Français du Sang-Occitanie (EFS), Inserm 1031, University of Toulouse, ERL5311 CNRS, National Veterinary School of Toulouse (ENVT), Toulouse, France.
5. Department of Medical Oncology, Institut Curie and Paris Sciences et Lettres Research University, 75005 Paris, France
6. Thoracic Oncology Department and Early Phase Unit CIC-1425, Hôpital Bichat, AP-HP, Université de Paris, 75018 Paris, France
7. Laboratoire PhysicoChimie Curie, Institut Curie, PSL Research University - Sorbonne Université – CNRS. Equipe labellisée Ligue Contre le Cancer ; 75005, Paris, France.
8. Department of Pathology, Institut Curie Hospital, 26, rue d'Ulm, F-75248 Paris, France.
9. Surgical Oncology Department, Institut Curie, PSL Research University, 75005 Paris, France
10. Translational Research Department, Institut Curie, PSL Research University, 75005 Paris, France
+ during the prepartion of this manuscript, our colleague Luc Sensébé passed away, may he rest in peace
** Present address: Songshan Lake Materials Laboratory, 523808 Dongguan, Guangdong (China)

Corresponding authors:

- Stéphanie Descroix: Stephanie.descroix@curie.fr
- and Jacques Camonis: JCamonis.Institut.Curie@gmail.com

Abstract:

Bone is the most frequent metastasis site for breast cancer. As well as dramatically increasing disease burden, bone metastases are also an indicator of poor prognosis. One of the main challenges in investigating bone metastasis in breast cancer is engineering *in vitro* models that replicate the features of *in vivo* bone environments. Such *in vitro* models ideally enable the biology of the metastatic cells to mimic their *in vivo* behavior as closely as possible. Here, taking benefit of cutting edge technologies both in microfabrication and cancer cell biology, we have developed *an in vitro* breast cancer bone-metastasis model. To do so we first 3D printed a bone scaffold that reproduces the trabecular architecture and that can be conditioned with osteoblast-like cells, a collagen matrix, and mineralized calcium deposition. We thus demonstrated that this device offers an adequate soil to seed breast cancer bone metastatic cells. In particular, patient-derived xenografts being considered as better approach than cell lines to achieve clinically relevant results, we demonstrate the ability of this biomimetic bone niche model to host patient-derived xenografted metastatic breast cancer cells. These patient-derived xenograft cells show a long term survival in the bone model and maintain their cycling propensity, and exhibit the same modulated drug response as *in vivo*. This experimental system enables access to the idiosyncratic features of the bone microenvironment and cancer bone metastasis, which has implications for drug testing.

Introduction

Cancer metastasis is a major evolutionary step in the natural history of cancer disease because it increases the burden of disease (through pain, invalidity, and other functional handicaps) and is also the cause of death for cancer patients, rather than the primary tumor [1,2]. A metastatic cancer is considered as a completely distinct disease with its own biology and metabolisms, as opposed to being interpreted as an ectopic colony of the primary tumor with identical biological properties [3].

The thorough study of the biology of metastasis faces many limitations, many of which are practical [4,5]. Experimental systems that tackle metastasis biology confront the same challenge as the biology of cancer in general, which is that establish an *in vitro* system respectful of the identity of initial cells. For instance, it is well known that in so-called "flat biology" cell lines that are derived from primary tumors and established in tissue culture plates vary in many aspects, including gene transcription, which has a huge impact on drug sensitivity [6-8]. Thus, new models or methods for cancer metastasis studies need to be developed. Several solutions have been proposed to address this issue, such as spheroids/organoids, tumor-on-chip, and mouse models, all of which have emerged as relevant experimental alternatives to study cancer-cell biology [9,10]. Nevertheless, these innovative methods also have unique limitations. While spheroids/organoids are better biomimetic 3D models than monolayer cultures, fibroblasts or immune cells are still deprived of the native tumor microenvironments that play essential roles during metastasis. Tumor-on-chips [11,12] and the use of some porous scaffolds [13,14] offer interesting 3D models that could provide interactions between cancer cells and stromal cells. However, most of them lack the physiological and mechanical architecture of the native environment, which are proven critical factors in bone metastasis [15-17]. The Achilles heel of mouse models is that they raise ethical problems regarding animal well-being, which is an issue that most countries refuse to ignore and are hardly representative of the autologous immune anti-cancer response in immune-compromised animals [6,7].

Bone metastases are among the most debilitating metastases (as they include pain, fracture, and medullary compression) and the most common metastatic site of invasive breast carcinomas [18-20]. In this context, we focus on the development of a new 3D breast cancer bone metastasis model, in which a biomimetic bone microenvironment can be maintained *in vitro* and metastatic breast tumor cells can be well settled and colonize the scaffold while maintaining their biological properties. We first reconstituted an *in vitro* bone niche with structural and mechanical features of trabecular bone using 3D printing; it was further refined by *in-situ* differentiating human bone marrow-derived mesenchymal stem cells (MSCs) into osteogenic lineage with collagen matrix and mineralized calcium depositions, which are critical in

bone homeostasis and regeneration [21-23]. To assess if this bone niche represents a bona fide soil to seed bone-metastasis cells, breast metastatic patient-derived xenograft (PDX) cells which are considered as better approach than cell lines to achieve clinically relevant results, were inoculated inside the bone. These co-cultures revealed that breast metastatic cells colonized the scaffold and replicated the cells' cycling proficiency, in a similar manner to *in vivo*. Finally, our study demonstrates that, in these conditions, metastatic breast cancer cells exhibit chemo-resistance, which could imply that this engineered breast cancer bone-metastasis model is a strong alternative for studying bone-metastasis pathophysiology.

Materials and methods

MSC culture and differentiation

Bone marrow mononuclear cells from healthy donors were obtained from femoral heads, according to the guidelines of the ethical committee of Toulouse University (N° AC-2014-2384). After Ficoll-gradient density separation, bone marrow MSCs were isolated from mononuclear cells that had been cultured in a basal culture medium: alpha-minimum essential medium (α-MEM) supplemented with 1% (100 U/mL/100 mg/mL) penicillin/streptomycin, 10% fetal bovine serum (FBS), and 1 ng/ml FGF2 (basic culture medium) [24]. After Passage 1, flow cytometry was performed to characterize the membrane phenotype of MSCs, as has been described elsewhere [25].

In order to evaluate their osteogenic potential, bone marrow MSCs were induced in an osteogenic differentiation medium in two steps, after one week of maintenance in a basal culture medium. Expanded MSCs were cultured in a Dex-diff medium (basal αMEM supplemented by 1% penicillin/ streptomycin, 10% FBS, 50 µM ascorbic acid, 10 mM β-glycerol phosphate, and 100 nM dexamethasone) for one week, and then in bone morphogenetic protein (BMP)-diff medium (basal α-MEM supplemented by 1% penicillin/streptomycin, 2% FBS, 50 µM ascorbic acid, 10 mM β-glycerol phosphate and 50 ng/mL BMP-4) for another week.

Reconstruction of a 3D-printed bone scaffold

The architecture of the bone scaffold was reconstructed from the trabecular part of the femoral epiphysis bone. First, a micro-tomography scanner was used to obtain the microstructure of the femoral epiphysis bone (Fig. 1a,b), with 10 µm Z resolution and 50 µm X,Y resolution [26]. Second, the threshold of the micro-tomography images was adjusted to remove the air or marrow from the interstitial spaces that filled the femoral epiphysis, but the bone microstructures were not removed (Fig. 1c). Finally, the image stacks of the bone microstructure were transformed into a 3D STL file using ImageJ. After reconstruction, a cylinder with 10 mm diameter and 2 mm height was selected (Fig. 1d) and further assembled with fiducials, in order to clarify the XYZ position for further characterization and to identify the pillars platform under the cylinder to avoid the first overexposure during 3D printing (Fig. 1e).

The assembled 3D bone scaffold file was loaded into a 3D stereolithography system (DWS 028J+, Italy). Bone scaffolds were then printed with 40 µm printing resolution in the Z-axis using DS-3000 biocompatible resin. Printed bone scaffolds were developed using isopropanol, dried under nitrogen stream, and cured for 12 minutes in a UV oven (DWS) (Fig. 1f). After UV exposure, the supporting pillar platform was

manually removed and the microstructures composing the bone scaffolds were characterized using SEM (S3700, Hitachi) (Fig. 1g). This demonstrated that the trabecular microstructures were replicated accurately, as has been described elsewhere [26]. Furthermore, the optical properties of the 3D-printed bone scaffolds were also checked by a confocal laser-scanning microscope (Leica SP8, Germany). DS-3000-based bone scaffolds have strong auto-fluorescence and absorption in the violet band (405 nm) but not in the blue, green, or far-red ranges (data not shown).

Prior to use, bone scaffolds were sterilized in 70% ethanol for 30 minutes. Then, the bone scaffolds were washed with PBS and further pre-treated with a basic culture medium every 24 hours for 48 hours. Finally, the pre-treated scaffolds were coated in 10 µg/mL human fibronectin overnight, before use.

MSC cultivation and differentiation in 3D-printed bone scaffolds

After pre-treatment and surface coating, bone scaffolds were inserted into 15 mL tubes for further MSC seeding and cultivation. Primary MSCs, which were those with less than five passages, were trypsinized and harvested in a basal culture medium at a density of 0.5 million/mL. Then, 2 mL MSC suspensions were added into each 15 mL tube that contained a bone scaffold, which were then gently agitated every ten minutes for the first 30 minutes and then every 30 minutes for a further 1.5 hours. Thereafter, 8 mL of the basic culture medium was added. The basic culture medium was renewed twice per week over the following three weeks (control conditions).

In parallel, MSCs were also induced into osteogenic lineage. After the seeding, which is described above, MSCs were cultured in a basic culture medium for one week and then differentiated by adding a Dex-diff medium after the first week and a BMP-diff medium after the second week. All mediums were renewed twice per week for three weeks (differentiated conditions). Meanwhile, MSCs were also osteo-differentiated in a Petri dish following the same procedure as described above.

Human breast cancer PDX dissociation and 3D *in vitro* culture

Since both triple-negative breast cancer (TNBC) and luminal B breast cancers (BMBC) can generate bone metastases [20], we tested the capacity of our bone-like niche to accommodate primary TNBC and bone metastases from BMBC.

TNBC PDX were established from a primary TNBC patient (HBCx-66) with residual disease after neoadjuvant chemotherapy [27], named HBCx-66 PDX. Meanwhile, BMBC PDX were established from fresh bone metastasis biopsies of estrogen receptor-positive breast cancer patients (HBCx-124 and HBCx-131), which progressed under endocrine treatment, named HBCx-124 PDX and HBCx-131 PDX. This was

in accordance with institutional guidelines and the rules of the Ethics Committee (project authorization no. 02163.02). Additionally, all patients signed the Institut Curie's institutional consent form that authorizes the use of medical records and biological specimens. Following this, both TNBC and BMBC PDX were dissociated and cultivated in the bone scaffolds, a 2D dish, and a Matrigel matrix. This was performed using the following method.

1. Breast cancer PDX dissociation

Fresh breast cancer PDX tissues were chopped into small pieces (~1 mm) with scalpels and further dissociated using a digestion medium that contained mouse collagenase (1 mg/mL) and hyaluronidase (1000 U/mL) for 45–60 minutes at 37 °C. Dissociated PDX cells were resuspended in the PDX culture medium (DMEM with 10% FBS, 1% P.S., 1% Pyruvate, 1% HEPES, 500 uL insulin, and 10 nM estrogen). Falcon® 100 µm cell strainers were used to remove the undigested tissue and PDX-derived tumor spheres that were larger than 100 µm. Several steps of washing were performed to remove single dead cells from PDX-cell suspensions. Then, Countess® Cell Counting Chamber Slides were used to quantify the concentration and viability of PDX cells.

2. Breast cancer PDX cell co-cultures in bone scaffolds and Petri dishes

After dissociation, two million breast cancer PDX cells were seeded into the bone scaffolds (both control and differentiated conditions) by gently shaking. In a similar manner as the MSC 3D seeding, 2 mL PDX cells (1 million/mL) were loaded into each 15 mL tube containing a bone scaffold and gently agitated every 15 minutes for the first 30 minutes and then every 30 minutes for the next 1.5 hours. After seeding, an 8 mL PDX culture medium was added. The PDX culture medium was renewed every two days for the next eight days.

Meanwhile, 0.5 million breast cancer PDX cells were also co-cultured with osteogenic-differentiated MSCs on 12-well plates, which acted as the 2D co-culture conditions. The PDX culture medium was not renewed, in order to avoid PDX cell detachment during the following eight days.

3. Breast cancer PDX cell cultures in Matrigel

In addition to being co-cultured in the bone scaffolds and 2D Petri dishes, the breast cancer PDX cells were cultured in a 3D Matrigel matrix to test the viability and proliferation proficiency of PDX cells *in vitro*. First, both glass-bottom multi-well plates and Nunc Lab-Tek II Chamber Slides, which were used for the 3D culture, were coated with a thick layer of the Matrigel matrix (>1 mm) and incubated for 20 minutes in an incubator. Then, 100µL breast cancer PDX cells were mixed in a final concentration of the Matrigel matrix and 1 million/mL were loaded onto the top of the thick Matrigel layer, which was then incubated for

another 45 minutes before the PDX culture medium was added. After incubation, the PDX culture medium was gently loaded, and PDX cells were cultured for seven days without the medium being changed.

TNBC PDX cell drug testing

Drug sensitivity was tested according to different culture conditions. Dissociated HBCx-66 PDX cells were seeded in 96-well plates at a density of 4×10^4 cells per well. After 24 hours, serially diluted cisplatin (0.01, 0.05, 0.1, 0.5, 1, 5, 10, 50, 100 [μM], NDC 67457-425-51, Mylan) was added by medium replacement for the next 72 hours of treatment. TNBC PDX cell viability was quantified using the CellTiter-Glo assay (Promega, G7570), while the dose-response curve and IC50 of cisplatin (2.4 μM) for inhibiting HBCx-66PDX cells was plotted by Prism software (Fig. SI3).

Subsequently, HBCx-66 PDX cells' response to cisplatin in the bone scaffolds and Matrigel was characterized using the following method. First, HBCx-66 PDX cells were seeded into the bone scaffolds and Matrigel in parallel, as previously described. After two days of culture, different final concentrations of cisplatin (2.4 μM [IC50 *in vitro*], 5.0 μM, and 10.0 μM) was added into the PDX cell culture medium by medium replacement every two days for the next four days of drug treatment. Here, the colonization and proliferation proficiency of HBCx-66 PDX cells in the bone scaffolds and Matrigel were characterized using the EpCAM area and Ki67 index, after drug treatment. Meanwhile, CellTiter-Glo 3D assays (Promega, G9682) were also used to evaluate the viability of HBCx-66 PDX cells in Matrigel with cisplatin treatment.

Statistical analysis

Results were presented as the mean ± standard error of the mean (SEM) for at least three repeated individual experiments for each group. Statistical differences were determined using Student's t-test for independent samples.

Results

Bioengineering a 3D biomimetic bone scaffold

To provide cancer cells with a 3D structure mimicking *in vivo* conditions, trabecular bone structures were first defined from µCT scan images. Then, a cylinder (ϕ=10 mm, H=2 mm) that faithfully replicates the trabecular bone structure was produced by stereolithography 3D printing. A biocompatible and visible light transparent photoresist, presenting stiffness of ~2×10^6 kPa (similar to native bulk bone), was used. The 3D printed scaffold replicates trabecular structures, with appropriate stiffness and pore sizes ranging from 100 to 500 µm, similarly to the native trabecular bone (Fig. 1) [26].

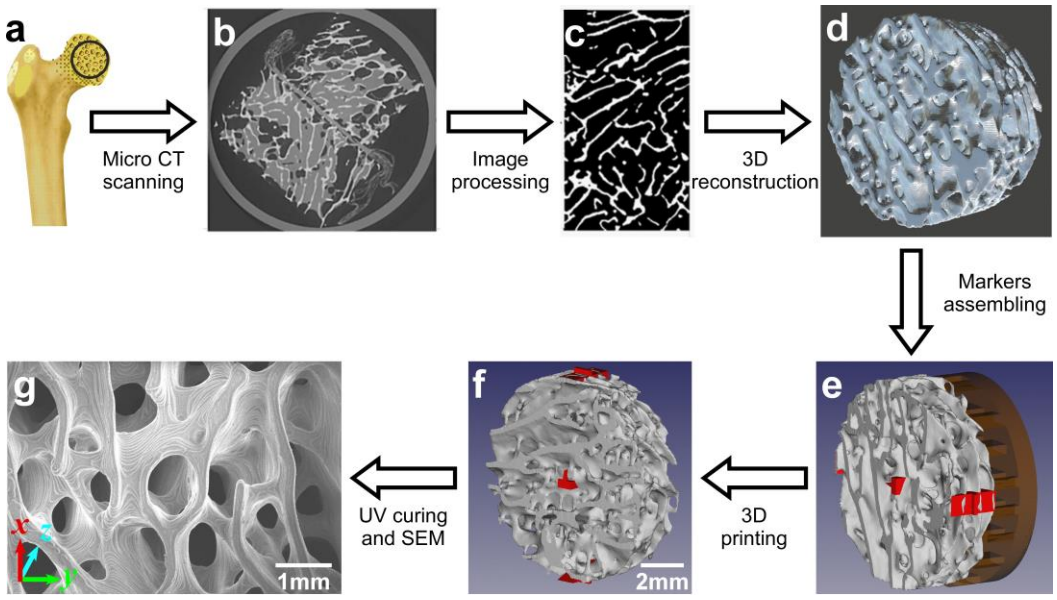

Fig.1 Reconstruction of bone scaffold by 3D printing.

A trabecular part of a leg bone was scanned by using micro-CT scanning **(a, b)**, and the CT images were converted and represented by using 3D modeling software (ImageJ, **c**). A randomly chosen cylinder zone with 10 mm in diameter and 2 mm in thickness **(d)** was assembled with pillar structures preserving the first layers melting of the bone structure during 3D printing and fiducials assisting 3D observation during single-photon confocal 3D scanning **(e)**. The bone scaffold made of resin (DS-3000) was printed **(f)**, cured by UV light, and characterized by using SEM (scanning electron microscopy) showing a smooth surface in XY plane and clear Z layer height (30 µm) along Z axis (**g**, top view, XY plane).

MSC proliferate and colonize the 3D printed bone scaffold

After pre-treatment and surface coating with fibronectin to promote cell adhesion, bone scaffolds were seeded with primary MSCs (10^6 MSCs) and basic culture medium. This was considered as Week "0." In order to evaluate MSC proliferation, living MSCs within each scaffold were stained with Cell Trace™ Yellow after the first, second, and third week of culture, and were imaged using a multi-field approach (Fig. 2a).

From the top view of the bone scaffold (Fig. 2b), the living MSCs gradually distributed and colonized the entire scaffold surface during the three-week culture. Even when the initial cell distribution was not completely uniform at the top of the structure (Fig. 2b), the top surface of the bone scaffold showed even coverage of living MSCs after three weeks of culture. The side view (Fig. 2b) reveals that the living MSCs also colonized the scaffold deep center.

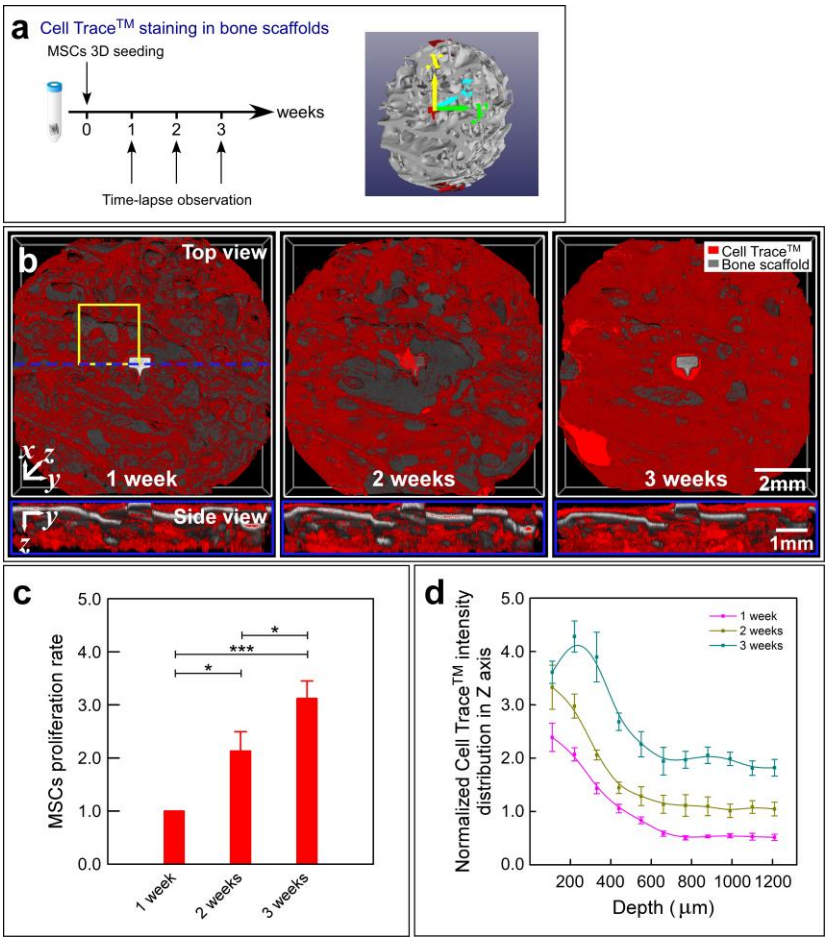

Fig.2 MSCs proliferation and colonization in 3D printed bone scaffold. (a) Primary MSCs were seeded in 3D printed bone scaffolds at "0" week. At 1st, 2nd, and 3rd week, MSCs were freshly stained with Cell Trace™ yellow respectively, and the living cell signals were collected by using the multi-field acquisition model of a confocal microscope. **(b)** Over-view of the Cell Trace™ stained MSCs (red) in the bone scaffold (gray) which were merged by 4×4 fields and reconstructed via image stacks (see materials and methods). Detailed MSCs distribution (in yellow box) during three weeks culture was shown in Movie SI1-3. **(c)** The proliferation rates of MSCs were validated as fold change of total whole-depth Cell Trace™ signal during three-week culture (see material and methods). **(d)** Normalized Cell Trace™ intensities (see material and methods) distribution along Z-axis (0-1200 μm) during 3D culture. The Cell Trace™ intensities at each depth position (averaged intensity of five adjacent frames from 0 to 1200 μm) were normalized to the Z-divided basal Cell Trace™ intensity and plotted along Z-axis. All results were obtained from independent experiments n≥3, the bars of graphics showed means ± standard error of the mean (SEM). * = $p<0.05$, **

= p<0.001, *** = p<0.0001, ns = not-significant, using unpaired Student t-test, and values were normalized to the first week.

Quantitatively, the proliferation index of MSCs was evaluated as the fold change of the total whole-depth Cell Trace™ signal, compared with first-week conditions. This showed a significantly increased total amount of MSCs in the bone scaffold during the three-week culture (Fig. 2c), with a proliferation index in the third week three times higher than the first week. We also evaluated MSC distribution along the Z-axis of the scaffold (SI Movies 1–3). Normalized Cell Trace™ intensity distribution along the Z-axis showed an increase in Cell Trace™ intensity over time, at each Z depth (Fig. 2d). Interestingly, these curves obtained in the first and third weeks have the same profile, which indicates that the MSC cells proliferate as rapidly in the deep center of the scaffold as on its surface, during the culture. These results suggest that MSCs can survive, proliferate, and colonize within the entire bone scaffold, and gradually become homogenously distributed across the scaffold surface over the course of the culture.

3D printed bone colonized with differentiated MSCs recapitulates bone features

In order to properly reconstruct a bone metastasis microenvironment, primary MSCs were induced to undergo osteogenic differentiation in bone scaffolds. Primary MSCs were seeded in bone scaffolds at Week “0” and then differentiated into osteoblastic cells by switching to a Dex-diff medium and BMP-diff medium at the end of the first and second weeks, respectively (see M&M and Fig. 3a). MSCs that were cultivated in the bone scaffolds with the basic culture medium for three weeks were considered a control experiment (Fig. 3a). In parallel, MSCs were also cultured and differentiated in a Petri dish, following the same procedure (Fig. SI4).

MSCs within the scaffolds were stained with Cell Trace™ Yellow, providing information about MSCs viability after osteogenic differentiation. The quantities of living MSCs, either in the whole scaffold or distributed along the Z-axis in the differentiated conditions, suggested that MSCs submitted to the differentiation procedure survived in, proliferated in, and colonized the whole 3D-printed bone scaffold (Fig. SI5).

The efficiency of osteogenic differentiation was thus evaluated by staining osteocalcin and collagen I, after which the IF value for each marker was characterized to quantify the osteogenic lineage commitment of MSCs and the extracellular-matrix deposition, respectively. 3D-reconstructed figures showed significantly increased signals of osteocalcin (Fig. 3b) and collagen I (Fig. 3d) in the differentiated conditions, compared with the control conditions. The distribution of osteocalcin and collagen I indexes along the Z-axis (see M&M) revealed that both indexes were higher in the differentiated conditions than in the control

conditions (Fig. 3c,e). In particular, the MSCs' osteocalcin index was ~4 times higher on the top surface and ~40 times higher at a depth of 1,000 μm, relative to the control conditions. Meanwhile, the collagen I index (Fig. 3e) was 3 times higher on the top surface and ~20 times higher at a depth of 1,000 μm in the differentiated conditions, compared to the control conditions. Furthermore, in the differentiated conditions, both osteocalcin and the collagen I index showed homogenous distributions along the Z-axis, while in the control conditions, these markers were mainly present at the surface. Taken together, these results demonstrate that MSC cells in the 3D-printed bone scaffold can undergo differentiation into osteoblast-like cells, with homogenously distributed osteocalcin expression and extracellular collagen I matrix deposition along the scaffold Z-axis. We also illustrated that there are no significant differences between the MSCs' nuclei area in the control and differentiated conditions (Fig. 3f), to further confirm that osteogenic-induced MSCs express more osteocalcin and collagen I in differentiated conditions.

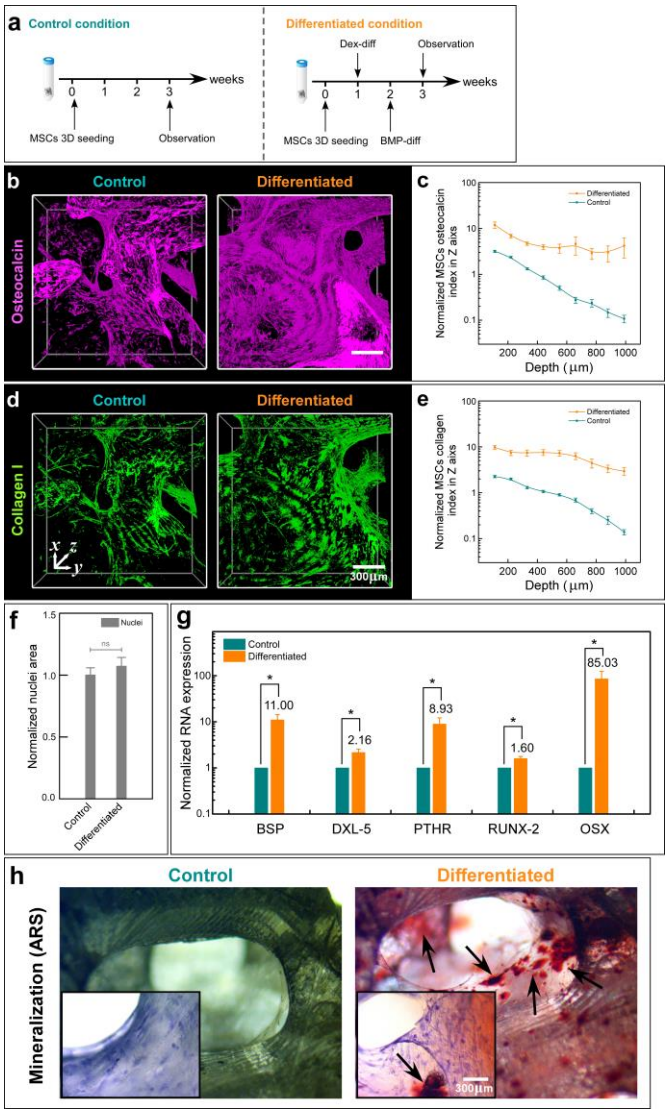

Fig.3 MSCs differentiation, collagen matrix deposition, and mineralization recapitulate a biomimetic bone. (a) Procedures of MSCs differentiation in 3D printed bone scaffold. For the differentiated conditions, primary MSCs were seeded and cultured in a bone scaffold at "0" week, followed by adding Dex-diff/BMP-diff medium at the end of first/second week separately for osteogenic differentiation. MSCs cultured with basic culture medium in a bone scaffold were considered as control conditions. **(b-f)** IF characterization of MSCs by staining with osteogenic markers (osteocalcin **(b)** and collagen I **(d)**) in the differentiated and control conditions. Reconstructed images of IF staining showed increased quantity of osteocalcin **(b)** and collagen I deposition **(d)** in the differentiated conditions compared to that in the control conditions. Correspondingly, normalized osteocalcin index (osteocalcin intensity per cell, see material and methods) and collagen I index (collagen deposition per cell, see material and methods) distribution along Z-axis (total 0-1000μm) were quantified (see material and methods). Quantification showed distribution of MSCs osteocalcin index **(c)** and collagen I index **(e)** in 1000μm depth in the control and differentiated conditions. **(f)** Nuclei area was measured for both the differentiated and control conditions, and it showed that there was no significantly difference between them. **(g)** Bone related genes expression was measured via RT-qPCR after MSCs 3D differentiation. mRNA levels of bone sialoprotein

(BSP), distal-less homeobox 5 (DLX5), parathyroid hormone receptor (PTHR), Runt-related transcription factor 2 (RUNX-2), and Osterix (OSX) of MSCs in both the differentiated and the control conditions were assessed. **(h)** Mineral depositions in both the differentiated and the control conditions were characterized by using Alizarin red s Staining method. Calcium deposition was observed in the differentiated conditions (red dots in the right panel) but not in the control conditions (left panel). All results were obtained from independent experiments n≥3, the bars of graphics showed means ± standard error of the mean (SEM). * = p<0.05, ** = p<0.001, *** = p<0.0001, ns = not-significant, using unpaired Student t-test, and values were normalized to control conditions.

In addition, when osteogenic differentiation was performed with MSCs grown in a 2D Petri dish, the MSC monolayer formed discontinuous, unstable clusters with more than 50% of MSCs detached from the surface (Fig. SI4), suggesting that the 3D-printed bone scaffold provides a more appropriate *in vitro* microenvironment to induce MSCs into osteogenic lineage.

In order to refine the above quantitative characterization of the osteogenic differentiation and to provide more evidence, we measured the expression levels of several genes involved in osteogenic differentiation (BSP, DLX5, PTHR, RUNX-2, and OSX mRNA species [28]) (Fig. 3g). All showed significant increases upon differentiation, particularly *OSX*, which increased 85 times. These results were consistent with the observed MSC osteogenic differentiation in Petri dish [25], indicating a *bona fide* osteogenic differentiation of MSCs in our bone scaffolds.

The ultimate stage of osteogenic differentiation leads to calcium deposition in the bone environment. In the bone scaffolds, mineralized calcium deposition was characterized using alizarin red S staining. Representative staining images showed widely distributed calcium mineralization in the differentiated conditions (Fig. 3h), whereas no signal was detected in the control conditions. This observation strongly suggests that our differentiated conditions replicated some features of an *in vitro* biomimetic bone.

Biomimetic bone niche maintains TNBC cells colonization and proliferation as *in vivo*

Since triple negative breast cancer (TNBC) is known to generate bone metastasis [20], we tested the capacity of our bone-like niche to accommodate primary TNBC cells. TNBC PDX were established from a primary TNBC patient with residual disease after neoadjuvant chemotherapy [27], named HBCx-66 PDX (Fig. 4a). HBCx-66 PDX cells were seeded into bone scaffolds, in which MSCs had been differentiated (Fig. 4a). As a control, similar experiments were performed using MSCs grown in a normal medium. In order to assess the advantage of our 3D bone niche, the same batch of HBCx-66 PDX cells was co-cultured with osteogenic-differentiated MSCs on a 2D Petri dish and in a 3D Matrigel without MSCs (Fig. 4a).

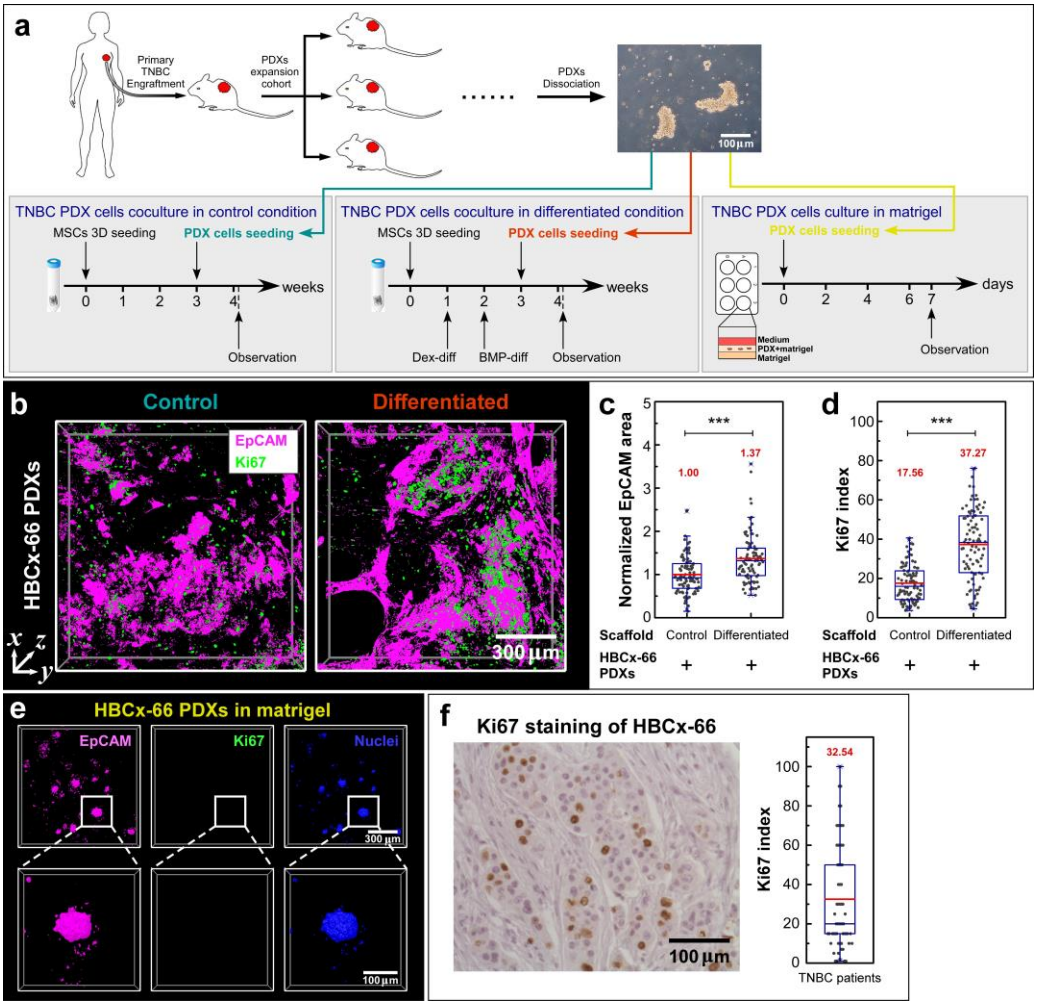

Fig.4 TNBC PDX colonization and proliferation in biomimetic bone scaffold. (a) Triple-negative breast cancer tissue (TNBC) from primary site was sectioned into small pieces and implanted into female nude mice to initiate and propagate TNBC PDXs. After several generations, TNBC (here, HBCx-66 PDXs) PDX tissue was dissociated and seeded into bone scaffolds (both control and differentiated conditions) and co-cultured for 8 days. As 3D *in vitro* control, the dissociated TNBC PDX cells were cultivated in Matrigel matrix for 7 days. **(b)** The colonization and proliferation capacity of HBCx-66 PDXs cells were characterized by staining with EpCAM (magenta) and Ki67 (green) markers respectively in both the control and differentiated conditions, and the 3D reconstructed images showed more EpCAM positive area and stronger Ki67 signal in differentiated conditions than in control conditions. **(c)** Quantification of normalized EpCAM area showed ~40% more of EpCAM positive area in the differentiated conditions than in control conditions. **(d)** quantified Ki67 index (defined as % of cancer nuclear area that is Ki67 positive, see Fig.SI2) and showed more than 2-fold increase of Ki67 positive PDX cells in the differentiated conditions than in the control conditions. **(e)** HBCx-66 PDX cells cultivated in Matrigel matrix were stained with EpCAM and Ki67 showing apparent EpCAM (magenta, left panel) and nuclei signals (blue, right panel) in HBCx-66 PDX cells but extremely rare Ki67 signal (green, middle panel). **(f)** Ki67 stained biopsy of HBCx-66 patient from the primary site of TNBC patients, and the statistical results from 62 TNBC patients showed a median Ki67 expression index (defined as % of cancer cells that are Ki67 positive) around 32%. The median values were shown by red bars and explicitly written above the points. All results were from

independent experiments n≥3, the bars of graphics showed means ± standard error of the mean (SEM). * = p<0.05, ** = p<0.001, *** = p<0.0001, ns = not-significant, using unpaired Student t-test, and values were normalized to co-cultured control conditions.

After eight days of co-culture, HBCx-66 PDX cells in the bone scaffolds were specifically identified by their epithelial marker EpCAM, while the Ki67 marker was used for proliferation characterization. We clearly observed more EpCAM and Ki67 positively stained HBCx-66 PDX cells in the biomimetic differentiated conditions than in control conditions (Fig. 4b). The EpCAM area and Ki67 index were thus calculated (Fig. SI2, see MM), we found an approximately 40% increase in the EpCAM-positive area (Fig. 4c) and more than a 110 % increase of the Ki67 index (Fig. 4d) for the differentiated conditions, compared to the control conditions. These results show that the HBCx-66 PDX cells performed better colonization, survival, and cycling proficiency in MSC osteogenic-differentiated conditions than in the bone scaffold that contained only undifferentiated MSC cells. In order to further assess the biological relevance of our bone-metastasis model, we investigated how this Ki67 index compares with an *in vivo* situation. Ki67 expression levels were quantified in a series of TNBC formalin-fixed paraffin-embedded (FFPE) samples for 62 TNBC patients. The median histopathology Ki67 index (indicating that 32% of cancer cells are Ki67 positive) (Fig. 4f) is similar to our biomimetic bone median Ki67 index (indicating that 37% of cancer-nuclear areas are Ki67 positive). This similarity suggests that our 3D-differentiated conditions actually provide a *bona fide* biomimetic microenvironment to maintain TNBC primary cells' cycling propensity *in vitro*.

TNBC PDX cells were also co-cultured with osteogenic-differentiated MSCs on a Petri dish for eight days and stained for EpCAM, Ki67, and nuclei. Unlike in the bone scaffolds, HBCx-66 PDX cells were rarely observed on Petri dishes, indicating that co-culturing with 2D-differentiated MSCs is insufficient for HBCx-66 PDX cell proliferation and colonization (Fig. SI6). The culture of cancer cells in Matrigel has been reported to better replicate some *in vivo* cancer-cell features, compared to 2D culture. However, after seven days of culture in the Matrigel, HBCx-66 PDX cells expressed EpCAM but only rarely were Ki67-positive signals observed (Fig. 4e).

Altogether, these results suggest that our bone scaffolds containing differentiated MSCs provided more biomimetic microenvironment than 2D cell culture, with a substantial increase in HBCx-66 PDX cell survival and colonization and provided improved microenvironment conditions, compared to Matrigel, by maintaining the high biological fidelity of HBCx-66 PDX proliferation during *in vitro* culture.

Biomimetic bone niche maintains bone-metastatic cells colonization and cycling propensity.

In order to further demonstrate the potential applications of the biomimetic bone niche to develop bone-metastasis models, we used cells derived from PDX that had been established directly from bone metastasis biopsies. In particular, these PDX had been established with bone metastasis samples from estrogen receptor-positive breast cancer patients, whose cancer had progressed under endocrine treatment. Following the same procedure that was outlined above, two types of bone-metastasis breast cancer (BMBC) PDX cells (HBCx-124 PDX and HBCx-131 PDX) were seeded and cultured in the bone scaffold, with both control and differentiated conditions, as well as in Matrigel (Fig. 5a).

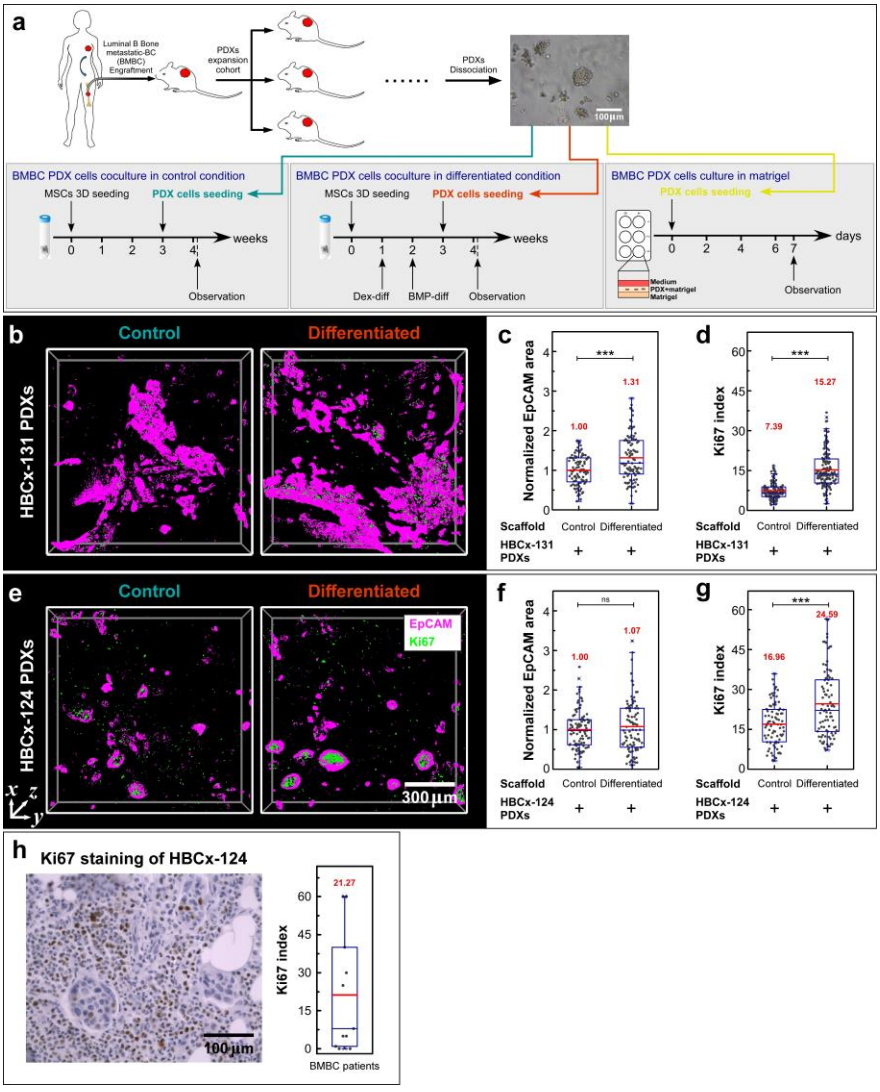

Fig.5 BMBC PDX cells represent the expression of Ki67 in biomimetic bone scaffold. (a) Luminal B breast cancer tissue from bone metastatic site (BMBC) was sectioned into small pieces and implanted into female nude mice to initiate and propagate BMBC PDXs. After several passages, dissociated BMBC PDX cells were seeded into both the control and differentiated conditions and then co-cultured for 8 days. The dissociated BMBC PDX cells were also cultivated in Matrigel matrix for 7 days as a 3D in vitro control. **(b,**

e) Two types of BMBC PDX cells (HBCx-124 PDXs and HBCx-131 PDX) were separately co-cultured in both control and differentiated conditions for 8 days followed by staining with EpCAM and Ki67. The reconstruction images of IF staining showed the 3D distribution of EpCAM area (magenta) and Ki67 (green) for both control and differentiated conditions. And corresponding quantification showed that the normalized EpCAM area was increased 31% and the Ki67 index was 2 times higher for HBCx-131 PDXs **(c,d).** Meanwhile, there was marginal increase of EpCAM area for HBCx-124 PDXs in differentiated conditions **(f)**, but there was 1.5 times higher Ki67 compared to the control conditions **(g)**. **(h)** Ki67 stained biopsy of HBCx-124 patient from the bone metastatic site of BMBC patients, and the statistical result from 11 BMBC patients showed a median Ki67 expression level around 21%. The median values are shown by red bars and explicitly written above the points. Results were from independent experiments n≥3, the bars of graphics showed means ± standard error of the mean (SEM). * = $p<0.05$, ** = $p<0.001$, *** = $p<0.0001$, ns = not-significant, using unpaired Student t-test, and values were normalized to control conditions.

Quantitative analysis of the HBCx-131 PDX cells grown in the 3D bone scaffold showed a 30% increase in the normalized EpCAM area and an increase of 105% for the Ki67 index in the differentiated conditions, compared to the control conditions (Fig. 5b,c,d). In the case of HBCx-124 PDX cells, we observed a marginal increase in the normalized EpCAM area and a 45% increase of the Ki67 index in differentiated conditions, compared with the control (Fig. 5e,f,g). The Ki67 expression level was also quantified for 11 BMBC patient samples, which retuned a median Ki67 expression level of around 21% relatively close to the values of BMBC PDX cells grown in our differentiated bone niche. These results suggest that, as previously shown for TNBC cells, the biomimetic differentiated conditions helped BMBC cells colonization and to maintain cells' cycling proficiency *in vitro*.

Additionally, both BMBC PDX cells were co-cultured with osteogenic-differentiated MSCs on Petri dishes, and rare PDX cells clusters survived for eight days (data not shown). Both BMBC PDX cells were also embedded in Matrigel, where EpCAM and nuclear signals were detected but no Ki67-positive cells (green) were observed (data not shown).

All these results suggest that, as with TNBC cells, our bone-like scaffolds provide a better biomimetic microenvironment that maintains the biological fidelity of BMBC cells during *in vitro* culture.

Modulated chemo-resistance to cis-platin of TNBC cells in biomimetic bone niche

Although our prior results are relevant to define adequate conditions for studying the biology of the bone metastasis of breast cancer, testing and predicting drug sensitivity or performing drug screening present other important applications.

Cisplatin is a common chemotherapy used for advanced TNBC patients with mitigated results underlining the need for refined preclinical evaluations. Cisplatin was applied to HBCx-66 PDX cells to measure the

cells' dose-response as a function of the biomimetic microenvironments. The viability of TNBC PDX cells was first quantified with a series of diluted cisplatin concentrations in a 96-well plate. A IC50 of 2.4 µM, which characterized the inhibition of TNBC PDX cells by cisplatin, was calculated from the dose-response curve (Fig. SI3).

The drug responses of HBCx-66 PDX cells to cisplatin in biomimetic 3D scaffolds were then measured (Fig. 6a, SI7a) using the following method. First, dissociated HBCx-66 PDX cells were seeded and co-cultured with MSCs in the scaffolds, in both control and differentiated conditions, and in Matrigel without MSCs for two days. Then, various concentrations of cisplatin were added (from 2.4 µM to 10 µM) by replacing the medium followed by four days of incubation.

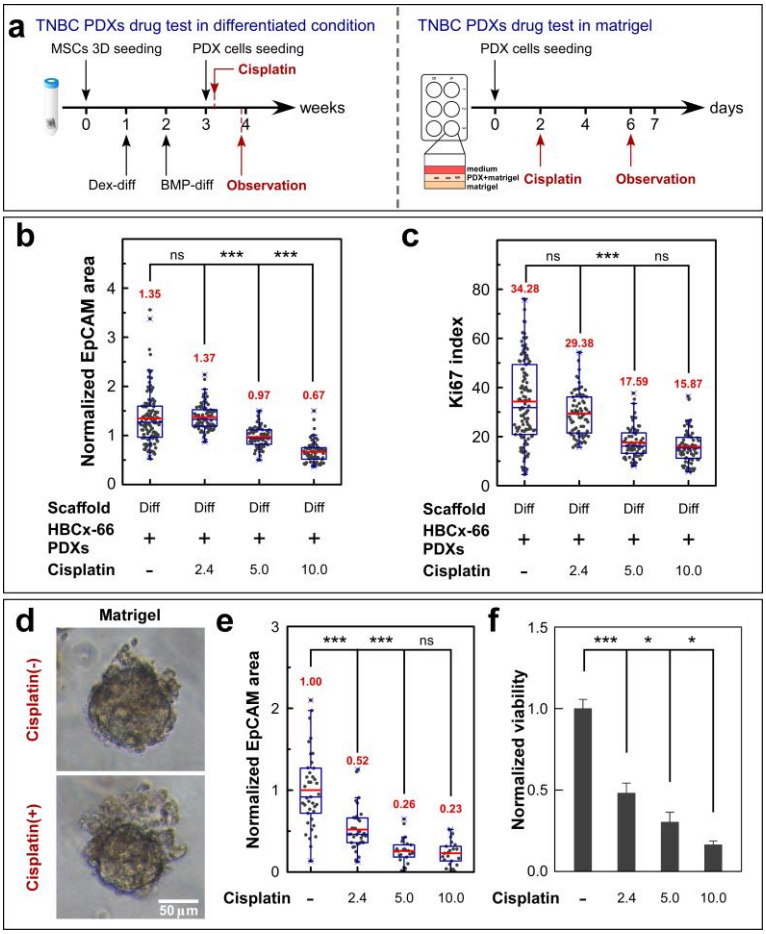

Fig.6 Biomimetic bone scaffolds promote chemo-resistance of TNBC PDX cells. (a) Drug response test of HBCx-66 PDX cells in bone scaffolds and Matrigel matrix. HBCx-66 PDX cells were seeded into both control (see Fig.SI6) and differentiated conditions and Matrigel matrix as previously described and cultivated 2 days followed by treatments with 2.4 µM (*in vitro* IC50), 5.0 µM, and 10.0 µM of cisplatin, separately, for 4 days. **(b,c)** normalized EpCAM area and Ki67 index were used to characterize the colonization and proliferation capacity of HBCx-66 PDX cells with and without cisplatin treatment in differentiated conditions (values were normalized to control conditions without drug treatment), respectively. And, more than 75 fields were measured and plotted in each condition. **(d)** Cisplatin treatment performed

(lower panel) or unperformed (upper panel) on HBCx-66 PDXs cells cultivated in Matrigel matrix. **(e)** normalized EpCAM area was also used to characterize the colonization capacity of HBCx-66 PDXs cells in Matrigel matrix (values were normalized to the condition in Matrigel matrix without drug treatment). Followed by EpCAM staining, normalized HBCx-66 PDXs EpCAM area showed a significant and continuous reduction with higher cisplatin concentration. **(f)** The viability of HBCx-66 PDXs cells in Matrigel was detected via Celltiter-Glo 3D assay with drug treatments (values were normalized to the condition in Matrigel matrix without drug treatment), and results showed that the decrease of HBCx-66 PDX cells viability was consistently with the decrease of HBCx-66 EpCAM area under the same cisplatin treatment. The median values are shown by red bars and explicitly written above the points. Results were from independent experiments n≥3, the bars of graphics showed means ± standard error of the mean (SEM). * = p<0.05, ** = p<0.001, *** = p<0.0001, ns = not-significant, using unpaired Student t-test.

As previously, the colonization and proliferation of HBCx-66 PDX cells in the scaffold were characterized by EpCAM and Ki67 staining in the presence or absence of cisplatin. In contrast to the results obtained in the 96-well plate, the normalized EpCAM area and Ki67 index of HBCx-66 PDX cells co-cultured in the 3D scaffold in differentiated conditions did not significantly decrease with 2.4 µM of cisplatin (Fig. 6b, c). A decrease of the EpCAM-positive area and a significant decrease of the Ki67 index were observed with 5 µM cisplatin treatment. By increasing cisplatin to 10 µM, the EpCAM-positive area decreased by around 50%, compared with the conditions without cisplatin, and the Ki67 index decreased from 34% to 16%. Meanwhile, although HBCx-66 PDX cells also presented a modulated drug response in control conditions, this was to a lesser extent (Fig. SI7b,c), which could have been caused by secreted factors of the MSCs' exposure to cisplatin [29].

In accordance with the results obtained in the 96-well plate, the EpCAM area of HBCx-66 PDX cells in the Matrigel matrix was reduced to 50% upon 2.4 µM of cisplatin, and continuously decreased with further increased cisplatin concentrations (Fig. 6d,e). Correspondingly, the viability of HBCx-66 PDX cells in the Matrigel matrix with cisplatin treatment, as estimated by CellTiter-Glo, showed a consistent decrease with increasing cisplatin concentrations (Fig. 6f).

These data indicate that the HBCx-66 PDX cells grown in biomimetic bone models exhibited modulated drug sensitivity to cisplatin, as 50% of HBCx-66 PDX cells were inhibited with 10 µM (equal to 3,000 ng/mL) cisplatin treatment, compared with 2.4 µM (equal to 720 ng/mL) in the 96-well plate or the Matrigel matrix. Such results are consistent with the clinical observations, which demonstrates that chemotherapy often failed to completely eliminate TNBC cells colonizing the bone, as evidenced by the clinical disease progression [30]. Furthermore, the results with 10 µM cisplatin in biomimetic bone models is not significantly different from the concentration of cisplatin (2000 ng/mL) in patients' steady-state serum [31], which suggests that biomimetic bone-metastasis models might access more physiological drug

response data *in vitro.* We could thus expect the sensitivity to drugs in our biomimetic bone model to adequately reflect *in vivo* sensitivity.

Discussion

To address the biology of the prevalent bone localization of many metastatic cancers, we need an adequate environment that replicates the *in vivo* environment conditions of metastatic cell growth and expansion. With the objective of bioengineering such an appropriate *in vitro* model of breast cancer bone metastasis, we first successfully established a biomimetic bone model that replicates some key features of an *in vitro* bone niche, particularly in terms of the native microstructures and stiffness of the trabecular bone and the presence of osteogenic-differentiated MSCs, a collagen I matrix, and mineralized calcium deposition. Compared with previously reported 3D bone models based on porous hydrogel and silk [13,14], our bone niche provides mechanical properties closer to the *in vivo* situation [17,26,32,33]. The scaffold stiffness is expected to enhance the adhesion of cells to the microstructure [32], while the spatial constraint allows cells to grow in a highly constrained space, as it does in bulk bone [32,34]. Our scaffold microfabrication presents several advantages, compared with decellularized bone scaffold [15] or fragmented mouse bones preloaded with breast cancer cells [35]. As demonstrated here with the trabecular bone [26], our model can faithfully replicate the bone microstructure and, if required, the geometrical parameters of the scaffold can be easily varied thanks to the 3D printing versatility. Regarding the model's biological applications, using 3D-printed scaffold remains advantageous because it allows experiments to be conducted in controlled and similar conditions. The 3D printed resist has demonstrated its compatibility with *in situ* optical characterization of cells a major asset compared to existing technologies [36] and its cytocompatibility has been shown suitable for cultivating and differentiating primary MSCs and PDX tumor cells. Even if this bone model does not fully replicate the real bone niche's complexity, it possesses the potential to address a wide range of biological issues related to complex cell–bone interactions.

Different tumor cell types are supposed to reproduce bone metastasis, each of which has its own pros and cons. Since PDX cells better maintain the important biological properties of parental tumors [37], these cells were chosen to validate our *in vitro* model of bone metastasis. To the best of our knowledge, this is the first time that TNBC and BMBC PDX were co-cultivated in such biomimetic bone models to reconstruct triple-negative and bone metastatic tumors in the bone microenvironment. Our 3D biomimetic bone model remarkably enhanced both the colonization properties and cycling proficiency of the TNBC PDX and BMBC PDX cells, compared to a 2D or 3D Matrigel culture. It is noteworthy that the

PDX cells' cycling proficiency (Ki67 index) maintained a similar level to that observed in patient samples. All these features align with the assumption that the bone microenvironment can inhibit apoptosis and promote tumor-cell proliferation [38-41]. Furthermore, we observed that TNBC PDX cells in biomimetic bone scaffolds showed a reduced drug response, compared with a conventional culture, which aligns with the known resistance of bone metastasis under the same treatment [42]. These results illustrate that critical components, such as the biomimetic tumor-cell co-culture in a biomimetic environment, could affect the bioavailability and/or efficacy of cisplatin [34,43]. Since cisplatin presented a strongly repeatable and modulated drug response in our biomimetic bone model, different chemotherapy drugs for metastatic breast tumors could be further tested.

Finally, the next step for this research could be to directly seed bone metastatic cells into our bone model after biopsy, with no PDX stage, in order to get closer to clinics. Moreover, as it has recently been reported that the metastatic bone microenvironment could modulate cancer's response to immunotherapy [44], our biomimetic bone model could also be used in the presence of immune cells to investigate how the bone microenvironment could modulate the tumor's response to immunotherapy.

Acknowledgments

This work was supported by the French RENATECH network. It was supported as part of the MultiFAB project funded by FEDER European Regional Funds and French Région Occitanie (grant agreement number 16007407/MP0011594) and by the HoliFAB project funded by the European Union's Horizon 2020 research and innovation program (grant agreement No 760927). This work has received the support of "Institut Pierre-Gilles de Gennes" (laboratoire d'excellence, Equipex, "Investissements d'avenir" program ANR-10-IDEX-0001-02 PSL and ANR-10-LABX-31-34). This work has been initiated and funded by Institut Curie PIC3I METABONE.

References

1. Gupta, G. P. & Massagué, J. Cancer Metastasis: Building a Framework. *Cell* **127**, 679–695 (2006).
2. Steeg, P. S. & Theodorescu, D. Metastasis: a therapeutic target for cancer. *Nat. Clin. Pract. Oncol.* **5**, 206–219 (2008).
3. Chiang, A. C. & Massagué, J. Molecular Basis of Metastasis. *N. Engl. J. Med.* **359**, 2814–2823 (2008).
4. Chaffer, C. L. & Weinberg, R. A. A Perspective on Cancer Cell Metastasis. *Science.* **331**, 1559–1564 (2011).

5. Talmadge, J. E. & Fidler, I. J. AACR Centennial Series: The Biology of Cancer Metastasis: Historical Perspective. *Cancer Res.* **70**, 5649–5669 (2010).
6. Hidalgo, M. *et al.* Patient-Derived Xenograft Models: An Emerging Platform for Translational Cancer Research. *Cancer Discov.* **4**, 998–1013 (2014).
7. Tentler, J. J. *et al.* Patient-derived tumour xenografts as models for oncology drug development. *Nat. Rev. Clin. Oncol.* **9**, 338–350 (2012).
8. Cheung, K., Gabrielson, E., Werb, Z. & Ewald, A. Collective Invasion in Breast Cancer Requires a Conserved Basal Epithelial Program. *Cell* **155**, 1639–1651 (2013).
9. Baker, B. M. & Chen, C. S. Deconstructing the third dimension-how 3D culture microenvironments alter cellular cues. *J. Cell Sci.* **125**, 3015–3024 (2012).
10. Pampaloni, F., Reynaud, E. G. & Stelzer, E. H. K. The third dimension bridges the gap between cell culture and live tissue. *Nat. Rev. Mol. Cell Biol.* **8**, 839–845 (2007).
11. Bhise, N. S. *et al.* Organ-on-a-chip platforms for studying drug delivery systems. *J. Control. Release* **190**, 82–93 (2014).
12. Nguyen, M. *et al.* Dissecting Effects of Anti-cancer Drugs and Cancer-Associated Fibroblasts by On-Chip Reconstitution of Immunocompetent Tumor Microenvironments. *Cell Rep.* **25**, 3884-3893.e3 (2018).
13. Reagan, M. R. *et al.* Investigating osteogenic differentiation in multiple myeloma using a novel 3D bone marrow niche model. *Blood* **124**, 3250–3259 (2014).
14. Qiao, H. & Tang, T. Engineering 3D approaches to model the dynamic microenvironments of cancer bone metastasis. *Bone Res.* **6**, (2018).
15. Villasante, A., Marturano-Kruik, A. & Vunjak-Novakovic, G. Bioengineered human tumor within a bone niche. *Biomaterials* **35**, 5785–5794 (2014).
16. Bissell, M. J. & Hines, W. C. Why don't we get more cancer? A proposed role of the microenvironment in restraining cancer progression. *Nat. Med.* **17**, 320–329 (2011).
17. Olechnowicz, S. W. Z. & Edwards, C. M. Contributions of the Host Microenvironment to Cancer-Induced Bone Disease. *Cancer Res.* **74**, 1625–1631 (2014).
18. Weilbaecher, K. N., Guise, T. A. & McCauley, L. K. Cancer to bone: a fatal attraction. *Nat. Rev. Cancer* **11**, 411–425 (2011).
19. Weigelt, B., Peterse, J. L. & van't Veer, L. J. Breast cancer metastasis: markers and models. *Nat. Rev. Cancer* **5**, 591–602 (2005).

20. Kennecke, H. *et al.* Metastatic Behavior of Breast Cancer Subtypes. *J. Clin. Oncol.* **28**, 3271–3277 (2010).
21. Bobbert, F. S. L. & Zadpoor, A. A. Effects of bone substitute architecture and surface properties on cell response, angiogenesis, and structure of new bone. *J. Mater. Chem. B* **5**, 6175–6192 (2017).
22. Kim, K., Yeatts, A., Dean, D. & Fisher, J. P. Stereolithographic bone scaffold design parameters: Osteogenic differentiation and signal expression. *Tissue Eng. - Part B Rev.* **16**, 523–539 (2010).
23. Sitarski, A. M., Fairfield, H., Falank, C. & Reagan, M. R. 3D Tissue Engineered in Vitro Models of Cancer in Bone. *ACS Biomater. Sci. Eng.* **4**, 324–336 (2018).
24. Brennan, M. A. *et al.* Inferior In Vivo Osteogenesis and Superior Angiogeneis of Human Adipose-Derived Stem Cells Compared with Bone Marrow-Derived Stem Cells Cultured in Xeno-Free Conditions. *STEM CELLS Transl. Med.* **6**, 2160–2172 (2017).
25. Naji, A. *et al.* Endocytosis of indium-tin-oxide nanoparticles by macrophages provokes pyroptosis requiring NLRP3-ASC-Caspase1 axis that can be prevented by mesenchymal stem cells. *Sci. Rep.* **6**, (2016).
26. Mézière, F. *et al.* Experimental observation of ultrasound fast and slow waves through three-dimensional printed trabecular bone phantoms. *J. Acoust. Soc. Am.* **139**, EL13--EL18 (2016).
27. Marangoni, E. *et al.* Capecitabine Efficacy Is Correlated with TYMP and RB1 Expression in PDX Established from Triple-Negative Breast Cancers. *Clin. Cancer Res.* **24**, 2605–2615 (2018).
28. Deschaseaux, F. *et al.* Regulation and function of immunosuppressive molecule human leukocyte antigen G5 in human bone tissue. *FASEB J.* **27**, 2977–2987 (2013).
29. Engler, A. J., Sen, S., Sweeney, H. L. & Discher, D. E. Matrix Elasticity Directs Stem Cell Lineage Specification. *Cell* **126**, 677–689 (2006).
30. Gobbini, E. *et al.* Time trends of overall survival among metastatic breast cancer patients in the real-life ESME cohort. *Eur. J. Cancer* **96**, 17–24 (2018).
31. Hellmann, M. D. *et al.* Preliminary safety, pharmacokinetics, and efficacy of regorafenib, cisplatin, and pemetrexed in patients with advanced nonsquamous non-small-cell lung cancers. *Clin. Lung Cancer* **16**, 514–522 (2015).
32. Marks, S. C. & Popoff, S. N. Bone cell biology: The regulation of development, structure, and function in the skeleton. *Am. J. Anat.* **183**, 1–44 (1988).
33. Lo, C.-M., Wang, H.-B., Dembo, M. & Wang, Y. Cell Movement Is Guided by the Rigidity of the Substrate. *Biophys. J.* **79**, 144–152 (2000).

34. Griffith, L. G. & Swartz, M. A. Capturing complex 3D tissue physiology in vitro. *Nat. Rev. Mol. Cell Biol.* **7**, 211–224 (2006).

35. Wang, H., Tian, L., Goldstein, A., Liu, J., Lo, .C., Sheng, K., Welte, T., Wong, S.T.C., Gugala, Z., Stossi, F., Zong, C., Li, Z., Mancini, M.A., Zhang, X.H.F., Bone-in-culture array as a platform to model early-stage bone metastases and discover anti-metastasis therapies. *Nat. Comm.* 8, 15045 (2017)

36. Bourgine, P. E., et al, In vitro biomimetic engineering of a human hematopoietic niche with functional properties, *Proc. Nat. Acad. Sci.*, **115** (25) E5688-E5695 (2018).

37. Siolas, D. & Hannon, G. J. Patient-derived tumor xenografts: Transforming clinical samples into mouse models. *Cancer Res.* **73**, 5315–5319 (2013).

38. Mundy, G. R. Metastasis to bone: causes, consequences and therapeutic opportunities. *Nat. Rev. Cancer* **2**, 584–593 (2002).

39. Kingsley, L. A., Fournier, P. G. J., Chirgwin, J. M. & Guise, T. A. Molecular Biology of Bone Metastasis. *Mol. Cancer Ther.* **6**, 2609–2617 (2007).

40. Calvi, L. M. *et al.* Osteoblastic cells regulate the haematopoietic stem cell niche. *Nature* **425**, 841–846 (2003).

41. Saidak, Z. *et al.* Extracellular calcium promotes the migration of breast cancer cells through the activation of the calcium sensing receptor. *Exp. Cell Res.* **315**, 2072–2080 (2009).

42. Zheng, H., Bae, Y., Kasimir-bauer, S., Coxon, A. & Lee, B. Therapeutic Antibody Targeting Tumor- and Bone Metastasis to Chemotherapy. *Cancer Cell* **32**, 731-747.e6 (2017).

43. Roodhart, J. L. *et al.* Mesenchymal Stem Cells Induce Resistance to Chemotherapy through the Release of Platinum-Induced Fatty Acids. *Cancer Cell* **20**, 370–383 (2011).

44. Jiao, S. *et al.* Differences in Tumor Microenvironment Dictate T Helper Lineage Polarization and Response to Immune Checkpoint Therapy. *Cell* **179**, 1177-1190.e13 (2019).